ELSEVIER

Advances in Water Resources 25 (2002) 147–157

Advances in Water Resources

www.elsevier.com/locate/advwatres

A forward particle tracking Eulerian–Lagrangian Localized Adjoint Method for solution of the contaminant transport equation in three dimensions

P. Binning [a,*], M.A. Celia [b]

[a] Department of Civil, Surveying and Environmental Engineering, The University of Newcastle, Callaghan, NSW 2308, Australia
[b] Department of Civil and Environmental Engineering, Princeton University, Princeton, NJ 08544, USA

Received 15 January 2001; received in revised form 23 September 2001; accepted 4 October 2001

Abstract

The contaminant transport equation is solved in three dimensions using the Eulerian–Lagrangian Localized Adjoint Method (ELLAM). Trilinear and finite volume test functions defined by the characteristics of the governing equation are employed and compared. Integrations are simplified by forward tracking of integration points along the characteristics. The resulting equations are solved using a preconditioned conjugate gradient method. The algorithm is coupled to a block-centered finite difference approximation of the groundwater flow equation similar to that used in the popular MODFLOW code. The ELLAM is tested by comparison with 1D and 3D analytic solutions. The method is then applied with random, spatially correlated hydraulic conductivities in a simulation of a tracer experiment performed on Cape Cod, Massachusetts. The linear test function ELLAM was found to perform better than the finite volume ELLAM. Both ELLAM formulations were found to be robust, computationally efficient and relatively straightforward to implement. When compared to traditional particle tracking and characteristics codes commonly used with MODFLOW, the ELLAM retains the computational advantages of traditional characteristic methods with the added advantage of good mass conservation.

1. Introduction

Contaminant transport problems are often difficult to solve numerically because of the mixed character of the governing equation, with particular difficulties associated with the hyperbolic part of the equation. Traditional finite difference and finite element methods are poorly suited for these problems, and often leave the user with a choice between nonphysical oscillations and excessive numerical diffusion. A number of modifications to the standard finite difference or finite element approach have been developed to reduce the problems, for example the flux corrected transport scheme [7], total variation diminishing scheme [20], streamline-upwind Petrov–Galerkin methods [28] and optimal test function methods [8]. However, these methods continue to be Eulerian in nature and are therefore limited by Courant number restrictions.

A second class of approximations is based on treatment of the hyperbolic part of the equation by a Lagrangian method, while the remainder of the equation is treated by an Eulerian-type of approximation. These methods include finite difference-based Eulerian–Lagrangian Methods [3], the Modified Method of Characteristics [14,15], and a variety of other related methods (for example [2,31,33,36]). While these methods overcome the Courant number restriction, most of them do not conserve mass, in part due to their inability to deal with general boundary conditions.

To overcome some of the limitations associated with these Eulerian–Lagrangian approximations, Celia et al. [9] introduced the Eulerian–Lagrangian Localized Adjoint Method (ELLAM). This method is similar to other Eulerian–Lagrangian methods, but has the advantages of global mass conservation (up to numerical integration errors) and a systematic and rigorous methodology for implementation of boundary conditions. The original ELLAM was presented for a 1D advection–diffusion equation with constant coefficients. Later, Herrera et al. [26] presented a theoretical framework for the development of the method. The method has since been

* Corresponding author. Tel.: +61-2-4921-5735; fax: +61-2-4921-6991.
E-mail addresses: pbinning@mail.newcastle.edu.au (P. Binning), celia@karst.princeton.edu (M.A. Celia).

0309-1708/02/$ - see front matter
PII: S0309-1708(01)00051-3

extended to include two spatial dimensions and variable coefficients [4,22,39], reaction terms [10,38] and nonlinear equations [1,11,13]. Wang et al. [39] presented a general ELLAM for arbitrary spatial dimensions, although no implementation was included. Other recent developments include a methodology for inclusion of point sources or sinks [23,40], and three initial reports on 3D implementations of the methodology [6,24,25].

In the present paper, we present a practical implementation of the ELLAM in three spatial dimensions and time. In the following section, we describe the governing equations being solved. This is followed by an outline of the ELLAM formulation, including details regarding both the trial and test functions being used, as well as details regarding evaluation of various integrals that arise in the formulation. This is followed by presentation of 1D and 3D test cases, in which the numerical approximation is compared to analytical solution. Finally, we apply the ELLAM to simulate a large-scale field experiment for which extensive data exist. This field-scale simulation, which includes a spatially variable, random hydraulic conductivity field, shows excellent agreement with field observations, thereby demonstrating the efficacy of the method. We finish the presentation with a general discussion of the methodology and some comments on future research directions.

2. Governing equation

In this paper, the ELLAM is applied to the advection–dispersion equation for the transport of contamination with concentration $c(\mathbf{x},t)$ in groundwater

$$L(c) = \frac{\partial(\phi c)}{\partial t} + \nabla\cdot(\mathbf{q}c) - \nabla\cdot(\phi\mathbf{D}\cdot\nabla c) = 0, \quad \mathbf{x}\in\Omega_x, \quad t\in(0,T],$$

where $\mathbf{D}$ is the dispersion tensor defined by

$$\mathbf{D}_{ij} = \alpha_T|\mathbf{v}|\delta_{ij} + (\alpha_L-\alpha_T)\frac{v_i v_j}{|\mathbf{v}|} + D_m\delta_{ij},$$

where $\phi(\mathbf{x})$ is the porosity, $\mathbf{q}$ the groundwater volumetric flux vector, α_L and α_T are the longitudinal and transverse dispersivities, $\mathbf{v}=\mathbf{q}/\phi$ is the groundwater velocity vector with components v_i, δ_{ij} is the Kronecker delta function, and D_m is the molecular diffusion coefficient.

The governing equation is subject to the boundary conditions

$$c(\mathbf{x},t) = g_1(\mathbf{x},t), \quad \mathbf{x}\in\partial\Omega_x^1, \quad t>0,$$

$$(-\mathbf{D}\cdot\nabla c)\cdot\mathbf{n}|_{\partial\Omega} = g_2(\mathbf{x},t), \quad \mathbf{x}\in\partial\Omega_x^2, \quad t>0,$$

$$(\mathbf{q}c-\phi\mathbf{D}\cdot\nabla c)\cdot\mathbf{n}|_{\partial\Omega} = g_3(\mathbf{x},t), \quad \mathbf{x}\in\partial\Omega_x^3, \quad t>0$$

and initial condition

$$c(\mathbf{x},0) = c_o(\mathbf{x}), \quad \mathbf{x}\in\Omega_x.$$

3. ELLAM formulation

The ELLAM is a method of weighted residuals and is formulated using the weak form of the governing equation

$$\int_0^\infty\int_{\Omega_x}\left(\frac{\partial(\phi c)}{\partial t} + \nabla\cdot(\mathbf{q}c) - \nabla\cdot(\phi\mathbf{D}\cdot\nabla c)\right)w(\mathbf{x},t)\,\mathrm{d}\mathbf{x}\,\mathrm{d}t = 0,$$

where $w(\mathbf{x},t)$ is a weighting or test function that will be defined later.

Integration by parts may be applied over space and time to yield

$$\begin{aligned}\int_0^\infty\int_{\Omega_x}\left(\frac{\partial(\phi c)}{\partial t} + \nabla\cdot(\mathbf{q}c) - \nabla\cdot(\phi\mathbf{D}\cdot\nabla c)\right)w(\mathbf{x},t)\,\mathrm{d}\mathbf{x}\,\mathrm{d}t &= -\int_0^\infty\int_{\Omega_x}\left(\phi c\frac{\partial w}{\partial t} + \mathbf{q}c\cdot\nabla w - (\phi\mathbf{D}\cdot\nabla c)\cdot\nabla w\right)\mathrm{d}\mathbf{x}\,\mathrm{d}t \\ &\quad + \int_0^\infty\int_{\partial\Omega_x}\mathbf{n}|_{\partial\Omega_x}\cdot[(\mathbf{q}c-\phi\mathbf{D}\cdot\nabla c)w]\,\mathrm{d}S\,\mathrm{d}t \\ &\quad + \int_{\Omega_x}[\phi c w]_0^\infty\,\mathrm{d}x, \end{aligned} \tag{1}$$

where $\mathbf{n}|_{\partial\Omega_x}$ is a unit vector normal to the spatial boundary $\partial\Omega_x$ of the global domain Ω_x.

The key to the ELLAM is definition of test functions w that satisfy the homogeneous adjoint equation locally,

$$L^*(w) = \phi\frac{\partial w}{\partial t} + \mathbf{q}\cdot\nabla w - \nabla\cdot(\phi\mathbf{D}\cdot\nabla w) = 0.$$

This can be achieved with an order-of-derivatives splitting [26]

$$\phi\frac{\partial w}{\partial t} + \mathbf{q}\cdot\nabla w = 0, \tag{2}$$

$$\nabla\cdot(\phi\mathbf{D})\cdot\nabla w = 0. \tag{3}$$

It is useful to introduce the material derivative defined by

$$\frac{\mathrm{D}}{\mathrm{D}t} = \frac{\partial}{\partial t} + \frac{\mathbf{q}}{\phi}\nabla.$$

With this definition and Eq. (2) it follows that $\mathrm{D}w/\mathrm{D}t = 0$.

3.1. Discretization

The time domain is partitioned into finite intervals of size $\Delta t^n = t^{n+1} - t^n$ and the 3D spatial domain is partitioned into rectangular cells. A block centered finite difference scheme is used to obtain the normal components of the flux vector $\mathbf{q}$ at the centers of the six faces of each cell. The concentration is determined at the eight corner nodes of each cell.

The ELLAM employs a finite number of space–time subdomains Ω^e, where $e = 1,2,\ldots,E$. A test function w_i is associated with each of the nodes $i = 1,2,\ldots,N$ and is

defined to satisfy Eqs. (2) and (3) locally within each subdomain. Eq. (3) is satisfied by any w_i that is piecewise constant within the subdomain Ω^e leading to a finite volume ELLAM [5,21]. If the material properties are homogeneous (porosity ϕ and dispersivity $\mathbf{D}$ are constant), then (3) is also satisfied by any w_i that is linear in $\mathbf{x}$. For linear functions, the assumption of homogeneity can (and will) be relaxed through careful evaluation of the integrals. Piecewise linear test functions have been described by Celia et al. [9] and others. Both formulations will be employed here and the resulting numerical methods compared.

3.2. Piecewise linear test functions

In the case of the linear test functions, the subdomains are defined to be a rectangular grid cell with vertices at the nodes at the new time level t^{n+1}. The grid cell is tracked backward in time to level t^n along characteristics defined by Eq. (2). The subdomain is bounded in time by the closed interval $[t^n, t^{n+1}]$ and in space by the 3D surface defined by backtracking the boundaries of the grid cells.

The test functions w_i are defined to be the Lagrangian piecewise tri-linear polynomial functions in space within the subdomain for $t \in [t^n, t^{n+1}]$. If the nodes are located at $\mathbf{x}_i$ $(i = 1, 2, \ldots, N)$ then w_i have the property that

$$w_i(\mathbf{x}_j, t^{n+1}) = \begin{cases} 1, & i = j, \\ 0, & i \neq j. \end{cases}$$

In each subdomain there are eight nonzero $w_i(x, t^{n+1})$ and they are linear in each coordinate direction.

3.3. Finite volume test functions

For the finite volume test functions, the subdomain is defined at t^{n+1} to be a rectangular parallelepiped centered at each node with sides bisecting space between the node and each of its 6 neighboring nodes. Where the node lies on the boundary, the boundary of the global domain forms a portion of the boundary of the subdomain. As with the linear test functions, the subdomain is tracked backward in time to time level t^n along the characteristics. The subdomain is then bounded in time by the closed interval $[t^n, t^{n+1}]$ and in space by the 3D surface defined by backtracking the boundary of the subdomain at t^{n+1}.

The test functions w_i are defined to be constant within each subdomain. If the subdomain Ω^i is centered at the node $\mathbf{x}_i (i = 1, 2, \ldots, N)$ then w_i are defined by

$$w_i(\mathbf{x}, t) = \begin{cases} 1, & \mathbf{x} \in \Omega^i, \\ 0, & \text{otherwise.} \end{cases}$$

These test functions are the so-called finite-volume test functions as described by Healy and Russell [21]. They have the property that mass is conserved both locally within each subdomain and globally. This property is in some ways desirable, although it has been observed to cause problems when the solution of the transport equation is coupled with a solution of the flow equation [5].

The finite volume test functions were also found by Healy and Russell [21] to give oscillations that are the result of the numerical integration scheme used in the evaluation of the integrals at the old time level. Healy and Russell employed "strategic integration points" to modify the definition of the test function and thereby control the oscillations.

3.4. Trial functions

The unknown concentration c is approximated in space by the piecewise tri-linear Lagrange interpolation functions defined with respect to the nodes $\mathbf{x}_i$

$$c(\mathbf{x}, t^n) \approx \hat{c}(\mathbf{x}, t^n) = \hat{c}^n(\mathbf{x}) = \sum_{j=1}^{N} C_j^n \psi_j(\mathbf{x}),$$

where $\hat{c}^n$ is the spatially piecewise tri-linear interpolant, and C_j^n is the approximation evaluated at spatial node j and discrete time level n. Notice that while the test functions are defined along the spatially complex domain defined along the characteristics at time n, the trial function is defined on the rectangular geometry of the spatial grid elements.

3.5. Evaluation of integrals

The integrals in Eq. (1) must now be evaluated. The development presented below applies to both the piecewise linear and finite volume test functions although the subdomains have different definitions in each case. Algorithmically, as the integrals are evaluated, the results are assembled in an algebraic equation of the form

$$\mathbf{A}\mathbf{c}^{n+1} = \mathbf{r}^n, \tag{4}$$

where $\mathbf{A}$ is the matrix of known coefficients that multiply the vector of unknowns $\mathbf{c}^{n+1}$, and $\mathbf{r}^n$ is a vector with entries depending on the known solution $\mathbf{c}^n$ and the known boundary terms.

To simplify evaluation of the spatial integrals the integrand is evaluated separately over each of the subdomains

$$\int_{\Omega_x} \mathrm{d}\mathbf{x} = \sum_{e=1}^{E} \int_{\Omega_x^e} \mathrm{d}\mathbf{x}.$$

The subscript x is used to emphasize that the integral is being evaluated over a spatial slice (at a given time) of the time-space subdomain Ω^e.

The test function w_i has been defined (2) so that $\mathrm{D}w_i/\mathrm{D}t = 0$ within the subdomain. However, there is a

jump discontinuity in Dw_i/Dt at the boundaries of the subdomain at the new and old time levels t^n and t^{n+1}. The theory of generalized functions as described in Gray et al. [18] can be used to evaluate the derivative

$$\frac{Dw_i}{Dt} = w_i^n(x)\delta(t-t^n) - w_i^{n+1}(x)\delta(t-t^{n+1}),$$

where δ is the Dirac delta function. On each subdomain Ω_x^e the integral (1) is then written

$$\begin{aligned}
&-\int_0^\infty \int_{\Omega_x^e} \left(\phi c \frac{Dw_i}{Dt} - (\phi \mathbf{D}\cdot\nabla c)\cdot\nabla w_i\right) d\mathbf{x}\,dt \\
&\quad + \int_0^\infty \int_{\partial\Omega_x} \mathbf{n}|_{\partial\Omega_x}\cdot[(\mathbf{q}c - \phi\mathbf{D}\cdot\nabla c)w_i]\,dS\,dt + \int_{\Omega_x^e} [\phi c w_i]_0^\infty \\
&= \int_{\Omega_x^e(t^{n+1})} \phi c^{n+1} w_i(\mathbf{x},t^{n+1})\,d\mathbf{x} - \int_{\Omega_x^e(t^n)} \phi c^n w_i(\mathbf{x},t^n)\,d\mathbf{x} \\
&\quad + \int_0^\infty \int_{\Omega_x^e} ((\phi\mathbf{D}\cdot\nabla c)\cdot\nabla w_i)\,d\mathbf{x}\,dt \\
&\quad + \int_0^\infty \int_{\partial\Omega_x} \mathbf{n}|_{\partial\Omega_x}\cdot[(\mathbf{q}c - \phi\mathbf{D}\cdot\nabla c)w_i]\,dS\,dt, \qquad (5)
\end{aligned}$$

where $[\phi c w_i]_0^\infty = 0$ for $t > 0$ by definition of w_i. The terms on the right-hand side must now be evaluated and these will be referred to as: the integral at the new time level; the integral at the old time level; the dispersion integral; and the boundary integrals, respectively.

3.5.1. Integral at new time level

In Eq. (5) the integral $\int_{\Omega_x^e(t^{n+1})} \phi c^{n+1} w_i(\mathbf{x},t^{n+1})\,d\mathbf{x}$ can be evaluated analytically as is done in a standard finite element formulation. This involves substitution of the trial function, $\hat{c}^{n+1}$, for c^{n+1}, and performance of the appropriate spatial integrations. Lumping can be employed if desired and will be shown to improve the solution. In the case of lumping, the integral is evaluated as

$$\begin{aligned}
&\int_{\Omega_x^e(t^{n+1})} \phi\hat{c}^{n+1} w_i(\mathbf{x},t^{n+1})\,d\mathbf{x} \\
&\quad \approx \phi\hat{c}(\mathbf{x}_i,t^{n+1}) \int_{\Omega_x^e(t^{n+1})} w_i(\mathbf{x},t^{n+1})\,d\mathbf{x} \\
&\quad = \phi C_i^{n+1} \int_{\Omega_x^e(t^{n+1})} w_i(\mathbf{x},t^{n+1})\,d\mathbf{x}.
\end{aligned}$$

3.5.2. Integral at old time level

The integral at the old time level t^n, $\int_{\Omega_x^e(t^n)} \phi c^n w_i(\mathbf{x},t^n)\,d\mathbf{x}$ is more difficult to evaluate because the domain $\Omega_x^e(t^n)$, defined by the characteristic tracking, does not correspond with the rectangular grid that defines $\hat{c}^n$. Two techniques for evaluating this integral appear in the literature. Binning and Celia [5] backtracked the subdomains to the old time level and evaluated the integrals analytically. This approach, while conceptually straightforward, presented severe computational difficulties due to the difficulty of designing algorithms to relate the geometry of $\Omega_x^e(t^n)$ to the regular grid. These difficulties were experienced in the 2D case and are expected to be much worse in the 3D case being considered here. Binning and Celia also only implemented the finite volume test functions, which are more straightforward than the case of piecewise linear test functions.

A more reasonable approach for higher dimensions was proposed by Healy and Russell [21,22]. They used numerical integration, defined at the old time level t^n, and tracked the integration points to the new time level along the characteristics. These locations are then used to determine the appropriate test function values, because the test functions are constant along characteristics, and they are defined with respect to the rectangular grid at time t^{n+1}. The algorithm can be described as follows. Firstly, partition the integral over the global domain Ω_x using the regular rectilinear grid $\Omega_x = \sum_{g=1}^{\text{grid cells}} G_g$ used to define the trial function $\hat{c}$. This grid has a regular geometry instead of the irregular geometry defined by the backtracked subdomains at the old time level t^n. The evaluation of the integral at the old time level can then be written in terms of the partition,

$$\sum_{e=1}^{E} \int_{\Omega_x^e(t^n)} \phi\hat{c}^n w_i(\mathbf{x},t^n)\,d\mathbf{x} = \sum_{g=1}^{\text{grid cells}} \int_{G_g} \phi\hat{c}^n w_i(\mathbf{x},t^n)\,d\mathbf{x}. \qquad (6)$$

Since each grid cell G_g has a regular geometry, we can cover it with P integration points $\mathbf{x}_p^g$ and known weights W_p^g ($p = 1,\ldots,P, g = 1,\ldots,\#$ grid cells). Then the integral (6) can be written

$$\begin{aligned}
&\sum_{g=1}^{\#\text{ grid cells}} \int_{G_g} \phi\hat{c}^n w_i(\mathbf{x},t^n)\,d\mathbf{x} \\
&\quad \approx \sum_{g=1}^{\#\text{ grid cells}} \sum_{p=1}^{P} (\phi\hat{c}^n(\mathbf{x}_p^g) w_i(\mathbf{x}_p^g,t^n) W_p^g).
\end{aligned}$$

In the above $\hat{c}^n(\mathbf{x}_p^g)$ can be evaluated by interpolation of the known solution. The test function $w_i(\mathbf{x}_p^g,t^n)$ is difficult to evaluate because the exact form of w_i is not known at t^n without carefully tracking the geometry of the subdomains from t^{n+1} to t^n. Instead of evaluating these complex geometries, the integration points are forward tracked to the new time level. Since w_i is defined to be constant along the characteristics it can be seen that

$$w_i(\mathbf{x}_p^g,t^n) = w_i(\mathbf{x}_p^{g^*},t^{n+1}),$$

where $\mathbf{x}_p^{g^*}$ is the coordinate of the point $\mathbf{x}_p^g$ forward tracked to the new time level t^{n+1}. If $\hat{c}^n(\mathbf{x}_p^g) = 0$ then it is not necessary to forward track the integration points, saving computational effort. The final approximation of the old time level integration is

$$\sum_{e=1}^{E}\int_{\Omega_x^e(t^n)}\phi\hat{c}^n w_i(\mathbf{x},t^n)\,\mathrm{d}\mathbf{x} \approx \sum_{g=1}^{\#\text{ grid cells}}\sum_{p=1}^{P}\phi\hat{c}^n(\mathbf{x}_p^g)w_i(\mathbf{x}_p^{g^*},t^{n+1})W_p^g.$$

To implement this sum in a computer algorithm, the procedure is as follows. For each grid cell g, forward track the integration points $\mathbf{x}_p^g$ to determine $\mathbf{x}_p^{g^*}$. At the new time level, note which $w_i(\mathbf{x}_p^{g^*},t^{n+1})$ are nonzero and add the term $\phi\hat{c}^n(\mathbf{x}_p^g)w_i(\mathbf{x}_p^{g^*},t^{n+1})W_p^g$ to the ith row of the right-hand side vector. In cases where the integration point is tracked through an outflow boundary, the point is not used in any of the evaluations, with the possible exception of certain outflow boundary conditions (which we do not consider herein).

3.5.3. Dispersion integral

The dispersion integral $\int_0^\infty\int_{\Omega_x^e}((\phi\mathbf{D}\cdot\nabla c)\cdot\nabla w_i)\,\mathrm{d}\mathbf{x}\,\mathrm{d}t$ is evaluated using a fully implicit approximation.

For the finite volume test functions there is a jump discontinuity at the edge of the subdomain. The derivative is evaluated using generalized functions [18] and the dispersion integral becomes

$$\begin{aligned}&\int_0^\infty\int_{\Omega_x^e}((\phi\mathbf{D}\cdot\nabla c)\cdot\nabla w_i)\,\mathrm{d}\mathbf{x}\,\mathrm{d}t\\&=-\int_{\partial\Omega^e}\left((\phi\mathbf{D}\cdot\nabla c)|_{\partial\Omega_i}\cdot\mathbf{n}|_{\partial\Omega_i}\right)\mathrm{d}S\,\mathrm{d}t\\&\approx\sum_{k=1}^{6}\Delta t A|_{\partial\Omega_i^{n+1}}^{k}(\phi\mathbf{D}\cdot\nabla\hat{c})\Big|_{\partial\Omega_i^k}^{n+1}\cdot\mathbf{n}|_{\partial\Omega_i^{n+1}}^{k}\end{aligned}$$

where the sum is over the six faces of the subdomain with area $A|_{\partial\Omega_i^{n+1}}^{k}$ at the new time level, and $(\phi\mathbf{D}\cdot\nabla\hat{c})|_{\partial\Omega_i^k}^{n+1}\cdot\mathbf{n}|_{\partial\Omega_i^{n+1}}^{k}$ is the component of $\phi\mathbf{D}\cdot\nabla\hat{c}$ normal to that side.

When tri-linear test functions are used

$$\begin{aligned}&\int_0^\infty\int_{\Omega_x^e}\left((\phi\mathbf{D}\cdot\nabla\hat{c})\cdot\nabla w_i\right)\mathrm{d}\mathbf{x}\,\mathrm{d}t\\&\approx\Delta t\int_{\Omega_x^e}((\phi\mathbf{D}\cdot\nabla\hat{c})\cdot\nabla w_i)^{n+1}\,\mathrm{d}\mathbf{x}\end{aligned}\qquad(7)$$

and the spatial integral on the right-hand side is evaluated analytically. Note that (7) does not rely on the assumption of homogeneous material properties required for (3) and so the linear ELLAM can be applied even when heterogeneous material properties are employed.

3.5.4. Boundary integrals

To complete the approximation the boundary term of Eq. (5)

$$\int_0^\infty\int_{\partial\Omega_x}\mathbf{n}|_{\partial\Omega_x}\cdot[(\mathbf{q}c-\phi\mathbf{D}\cdot\nabla c)w_i]\,\mathrm{d}S\,\mathrm{d}t\qquad(8)$$

must be evaluated. Here we describe only inflow boundaries. For outflow boundaries, it is assumed that either a Dirichlet boundary condition is specified and the ELLAM equation at the boundary is replaced by the statement of the boundary condition, or a zero total flux is specified and (8) can be neglected. Procedures for evaluating more general outflow boundaries have been described by Healy and Russell [22], Russell and Trujillo [34] and Wang et al. [37] amongst others.

Inflow boundaries are evaluated using numerical integration. The forward tracking procedure avoids the necessity to explicitly define boundary test functions [9]. The total area of the global domain boundary is divided into subdomains consistent with the spatial partitioning of the rectangular grid. Let E denote the number of these subdomains, or subareas, along the spatial boundary. In each of these subareas the integral in (8) is evaluated with P integration points along the spatial portion of the boundary, with weights W_p^e, and Q integration points in time with weights W_q^e. The resultant approximation is then

$$\begin{aligned}&\int_0^\infty\int_{\partial\Omega_x}\mathbf{n}|_{\partial\Omega_x}\cdot[(\mathbf{q}c-\phi\mathbf{D}\cdot\nabla c)w_i]\,\mathrm{d}S\,\mathrm{d}t\\&\approx\sum_{e=1}^{E}\sum_{q=1}^{Q}\sum_{p=1}^{P}\mathbf{n}|_{\partial\Omega_x}\cdot[(\mathbf{q}c-\phi\mathbf{D}\cdot\nabla c)w_i]|_{\mathbf{x}_p}^{t_q}W_p^eW_q^e.\end{aligned}$$

The evaluation of the sum on the right-hand side and its placement in the algebraic Eq. (4) depends on the boundary condition type at $(\mathbf{x}_p,t_q)$.

If the total flux $\mathbf{n}|_{\partial\Omega_x}\cdot[(\mathbf{q}c-\phi\mathbf{D}\cdot\nabla c)w_i]|_{\mathbf{x}_p}^{t_q}$ is given then it is only necessary to find $w_i(\mathbf{x}_p,t_q)$ to evaluate the sum, which is then placed in the right-hand side vector $\mathbf{r}^n$. A method similar to that employed for the old time level integrations is used. The integration point $\mathbf{x}_p$ at time t_q is tracked forward to $\mathbf{x}_p^*$ at t^{n+1} and then $w_i(\mathbf{x}_p,t_q)$ can be found by noting that $w_i(\mathbf{x}_p,t_q)=w_i(\mathbf{x}_p^*,t^{n+1})$.

If the concentration $c(\mathbf{x}_p,t_q)$ is given as the boundary condition, then $w_i(\mathbf{x}_p,t_q)$ is evaluated as for a total flux condition and $\mathbf{n}|_{\partial\Omega_x}\cdot[(\mathbf{q}c)w_i]|_{\mathbf{x}_p}^{t_q}$ is placed in the right-hand side vector $\mathbf{r}^n$. The term $\mathbf{n}|_{\partial\Omega_x}\cdot[(\phi\mathbf{D}\cdot\nabla\hat{c})w_i]|_{\mathbf{x}_p}^{t_q}$ is unknown and is evaluated by projecting to the new time level

$$\mathbf{n}|_{\partial\Omega_x}\cdot\left[(\phi\mathbf{D}\cdot\nabla\hat{c})w_i\right]\Big|_{\mathbf{x}_p}^{t_q}\approx\mathbf{n}|_{\partial\Omega_x}\cdot\left[(\phi\mathbf{D}\cdot\nabla\hat{c})w_i\right]\Big|_{\mathbf{x}_p^*}^{t^{n+1}}.$$

Boundary conditions of known concentration gradient are not considered here but can be treated using similar techniques to those presented for the total flux and known concentration boundary conditions.

The number of boundary integration points Q must be selected carefully in order that the boundary term is sufficiently resolved. In all examples presented in this paper, the number of boundary points Q is computed from the number of spatial integration points P and the Courant number $Cr=|\mathbf{v}|\Delta t/\Delta x$, (where $|\mathbf{v}|$ is the velocity

and Δx is the grid spacing) with $Q = P * Cr$. Thus, increasing the time step size to allow fewer time steps does not lead to a strictly proportionate reduction in computational effort because the use of larger time steps leads directly to a requirement for a greater number of boundary integration points and a consequent increase in computations required for the matrix assembly. This is consistent with the increased importance of boundary information when the time step is large. However, the use of larger time steps means that fewer matrix inversions and evaluations of the interior integrals (5) are required. As a result, there is a significant computational saving when large time steps are used.

3.6. Tracking procedure

Forward tracking of integration points is accomplished by the semi-analytic method described by Goode [17] and Healy and Russell [21]. The velocities are given at the intercell boundaries and are assumed to be constant over the time step while varying linearly in space across each cell. In this paper the velocities are provided by a block centered finite difference solution of the groundwater flow equations. The solution of the flow equation is similar to that employed in the USGS code MODFLOW [19].

The tracking algorithm employs a one point temporal approximation to velocity. This will lead to errors in cases where the velocity is highly variable in time. In this case a higher order approximation should be used in the forward tracking procedure. For the examples presented herein, we use a steady-state velocity field, so a constant-in-time velocity is appropriate.

3.7. Solution of matrix equation

The matrix **A** in Eq. (4) is asymmetric (due to the boundary conditions) and the algebraic equations are solved by a conjugate gradient squared algorithm.

4. Results

4.1. 1D test problem

The particle tracking ELLAM with both finite volume and linear test functions is compared to the analytical solution of Ogata and Banks [32] and an implicit Galerkin finite element method with linear basis and test functions. The problem is solved on the domain $x \in [0,1]$ with equation parameters $\alpha = 0.01$, $v = 0.7$, boundary conditions $c(0,t) = 1.0$, $c(1,t) = 0.0$ and initial condition $c(x,0) = 0$.

The domain is discretized using both a coarse grid ($\Delta x = 0.1$) and a fine grid ($\Delta x = 0.01$). A single small grid cell $\Delta x = 0.0001$ is employed next to the inflow boundary so that the step concentration change of the Ogata and Banks solution is represented accurately in the numerical simulations. Shown in Fig. 1 are the solutions using various methods at $t = 0.6$. The ELLAM solutions were all obtained with a single time step while the finite element solution required 60 time steps. The ELLAM solutions employed two Gaussian numerical integration points ($P = 2$) per element and $Q \approx P \times Cr$ integration points on the inflow boundary. This resulted in $Q = 8$ and $Q = 80$ for the 10 and 100 element simulations, respectively. All simulations are shown using consistent (or unlumped) matrix evaluations at t^{n+1}.

As can be seen from Fig. 1, the ELLAM does a reasonable job of finding the solution with only a single time step. In contrast, the finite element method required 60 time steps (with $\Delta x = 0.01$) to achieve a similar accuracy. This result demonstrates the computational efficiency of the ELLAM. The poor performance of the finite element method is due to the necessity of restricting the time step size to obtain a solution.

For this problem, both the ELLAM and the finite element method are perfectly mass conserving. Compared to the finite element solution, the ELLAM exhibits much smaller artifacts due to numerical diffusion. In fact, when only one time step is used the ELLAM under predicts the physical dispersion. This is because a fully implicit time stepping procedure has been used and the diffusive flux is proportional to the gradient in concentration. This gradient is much smaller at the end of the time step than at the beginning so that the diffusive flux is under predicted. When more ELLAM time steps are taken, the solution improves because the diffusive flux is more accurately estimated.

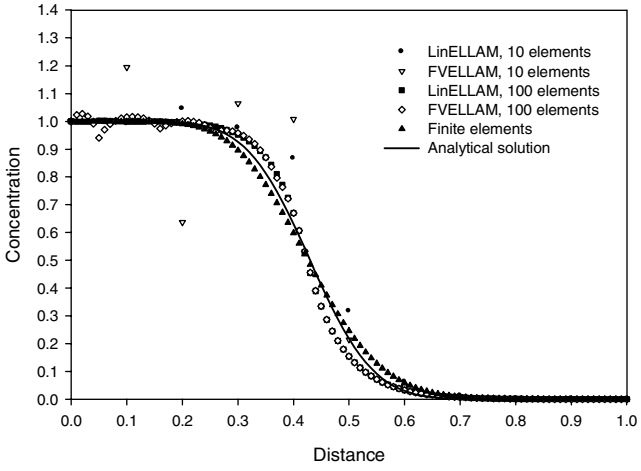

Fig. 1. Comparison of the ELLAM with linear test functions (LinELLAM) and the finite volume ELLAM (FVELLAM) with the 1D analytical solution of Ogata and Banks [32] and a Galerkin Finite element solution.

On the other hand, the finite element solution adds numerical diffusion at every time step. The ELLAM adds numerical diffusion due to interpolation error in the evaluation of the integral at the old time level. Because the ELLAM requires fewer time steps to find the solution, the numerical diffusion in the ELLAM is much smaller.

Both the finite volume ELLAM and the linear ELLAM are shown in Fig. 1. When employing the finite volume ELLAM either the domain must be finely discretized or a sufficient number of integration points must be chosen. In Fig. 1, for example, the FVELLAM displays oscillations when two numerical integration points ($P = 2$) are used. These oscillations can be controlled by employing additional integration points at added computational cost. The requirement for a dense cover of integration points when employing the finite volume test functions was noted by Healy and Russell [21] who resolved the problem by modifying the finite volume test functions to reduce the effect of the jump discontinuities in the function. A simpler approach is to use piecewise linear test functions. As shown in Fig. 1, even with only two integration points the solution is quite well behaved. The use of piecewise linear test functions avoids the need for the Strategic Spatial Integration Points introduced by Healy and Russell.

4.2. Comparison with 3D analytical solution

To demonstrate the accuracy of the method in three dimensions, the linear and finite volume ELLAM are compared with the 3D analytic solution of Leije et al. [30]. The domain is a rectangular block of size $10 \times 5 \times 5$ in the x, y, z directions, respectively and is discretized into uniform blocks of size $\Delta x = \Delta y = \Delta z = 0.5$. The numerical solution is found using a single time step of size $\Delta t = 6$. The velocity field in the domain is unidirectional in x with $(v_x, v_y, v_z) = (0.7, 0, 0)$ and is chosen so that the Courant number $Cr = v_x \Delta t / \Delta x$ is not an integer. If integer values of the Courant number are used then the ELLAM is more accurate because interpolation errors in the integral at the old time level $\int_{\Omega_x^e(t^n)} \phi c^n w_i(\mathbf{x}, t^n)\, d\mathbf{x}$ are minimized. Because the Courant number cannot be regulated in heterogeneous problems we select $Cr \neq 1$ to fully illustrate any model errors. The domain is initially free of contaminant $c(t = 0) = 0$ and contaminant is injected with a fixed concentration $c = 1$ from a 2D y–z patch of size 1.5×1.5 located at the inflow end of the domain. All other sides are set to be no flux boundaries to contaminant. The dispersivities are set to be $\alpha_L = 0.01$ and $\alpha_T = 0.001$.

The problem is solved with both the linear and finite volume ELLAM using various spatial grids, different numerical integration schemes and both temporally consistent and lumped formulations. The numerical solution is compared with the analytical solution at $t = 6$ in Table 1. All simulations were obtained with only a single time step. The root-mean-squared (RMS) error shown in the table is given by

$$\text{RMSError} = \frac{1}{n}\sqrt{\sum_i (c_i^m - c_i^a)^2}$$

and the maximum error by

$$\text{MaxError} = \max_i |c_i^m - c_i^a|.$$

The results show that quite accurate solutions can be obtained with the ELLAM even when a coarse spatial and temporal discretization has been employed. The Linear ELLAM is superior to the finite volume ELLAM

Table 1
Comparison of the ELLAM with the analytical solution of Leije et al. [30]

Type	Δx	P	Q	Lumped	RMSError	MaxError
LinELLAM	0.5	1	10		6.78×10^{-4}	0.417
	0.5	2	20		5.93×10^{-4}	0.334
	0.5	4	40		5.85×10^{-4}	0.285
FVELLAM	0.5	1	10		6.67×10^{-3}	8.718
	0.5	2	20		9.83×10^{-4}	0.594
	0.5	4	40		5.27×10^{-4}	0.240
LinELLAM	0.5	1	10	√	2.11×10^{-4}	0.0905
	0.25	1	20	√	5.23×10^{-5}	0.0942
	0.1	1	50	√	1.06×10^{-5}	0.1043
	0.5	2	20	√	1.39×10^{-4}	0.0909
	0.5	4	40	√	1.24×10^{-4}	0.0830
FVELLAM	0.5	1	10	√	4.15×10^{-3}	5.205
	0.25	1	20	√	1.02×10^{-3}	4.823
	0.1	1	50	√	1.35×10^{-4}	4.105
	0.5	2	20	√	6.28×10^{-4}	0.253
	0.5	4	40	√	2.81×10^{-4}	0.142

when a small number of integration points is employed. However, the methods have similar accuracy when sufficient integration points are used. Lumping improves both the linear and finite volume ELLAM. However, these results are specific to this test case. The conclusion that lumping is preferable should be made with caution since lumping introduces numerical diffusion that may increase errors despite the benefit of controlling oscillations [12].

The results also demonstrate that the solution converges as the grid is refined with second order spatial accuracy achieved in both the linear and finite volume ELLAM. Note, however, while the RMS error decreases with grid refinement, the max error does not change appreciably as the grid is refined. This is because of numerical errors introduced by employing a one point temporal approximation of the dispersion term. This is a limitation of the current ELLAM formulations where the emphasis is placed on accurately resolving the advection component of the equation with minimum computational cost.

In summary, to obtain computationally efficient and accurate solutions, the lumped Linear ELLAM with a smaller number of integration points appears to be a good choice for these types of simulations.

4.3. 3D random fields simulation

To demonstrate the robustness and practical utility of the new 3D ELLAM code, it is used to simulate the Cape Cod tracer experiment described by LeBlanc and others [16,27,29]. In this experiment, a bromide tracer was injected into an unconfined aquifer formed from a glacial outwash. The tracer was observed for 511 days in a network of 656 multilevel sampling wells. The spatial moments of the observed contaminant distribution were calculated and stochastic groundwater theory used to estimate the macrodispersivity of the aquifer. Herein, a single random conductivity field simulation of the Cape Cod experiment is presented to demonstrate the practical use of the ELLAM. It is shown that random field transport simulations can be efficiently obtained and used with stochastic theories in the same way as the field data. Since analytical solutions are not available for these simulations, only a few comments on the accuracy of the numerical method are made.

In the experiment, a bromide tracer was injected in 3 wells perpendicular to the flow, resulting in a contaminant plume of initial concentration 640 mg/l and dimensions estimated to be $4 \times 4 \times 1.2$ m^3 located between 1.2 and 2.4 m below the water table. Because of the chosen spatial discretization, the initial contaminant mass in the plume is 4792 g, slightly less than the mass of 4900 g used in the actual tracer experiment. The head at the wells was 13.80 m, while 50 m downstream the head was 13.72 m. The material properties of the aquifer have been well documented and are simulated here as a random field generated by the turning bands algorithm [35]. Table 2 and Fig. 2 summarize these properties. The dispersivity employed in the simulation is the Cape Cod local scale dispersivity calculated by Zhang et al. [42] from the column experiment data of Wood and Kraemer [41]. Since the transverse dispersion cannot be obtained from the published 1D laboratory column experiments, a value of $\alpha_T = 1/10\alpha_L$ is assumed. A $50 \times 20 \times 50$ grid with $1\text{ m} \times 1\text{ m} \times 0.1\text{ m}$ cells was employed with $P = 2$ integration points per subdomain and $Q = 5$. A second simulation using a refined $100 \times 40 \times 100$ grid with $P = 2$, $Q = 10$ was also run. In both cases, a time step of 200 h was used in the simulations so that 10 time steps were used over the duration of the simulation. The choice of time step size was dictated by the desire to obtain model output at frequent intervals during the simulation. However, it is possible to obtain a solution with as few as 2 time steps.

The flow field was simulated at steady state and Figs. 3 and 4 show the distribution of contamination initially, and at 1000 and 2000 h, for the coarse grid. The velocity of the simulated contaminant plume is calculated from the first moments of the solution and found to be 0.341

Table 2
Parameters used in the simulation of the Cape Cod field experiment

Mean K	3.96 m/h
Variance of ln (K)	0.24
Vertical correlation length	0.19 m
Horizontal correlation length	3.5 m
Porosity	0.39
α_L	2.58×10^{-3} m
α_T	2.58×10^{-4} m
Retardation factor	1
$\Delta x = \Delta y$	1 m
Δz	0.1 m
Δt	200 h

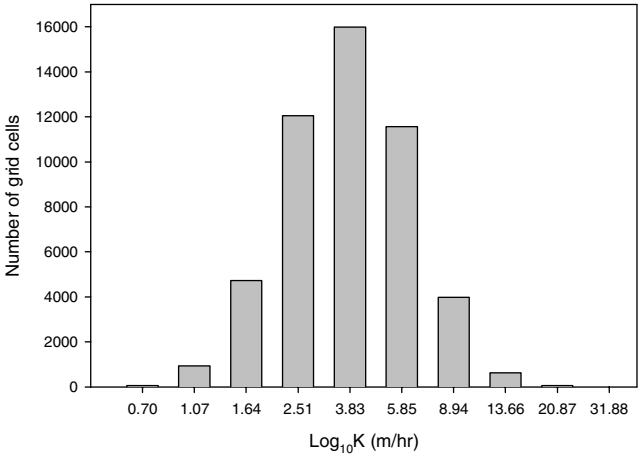

Fig. 2. Distribution of conductivity used in the random field simulation of the Cape Cod field experiment.

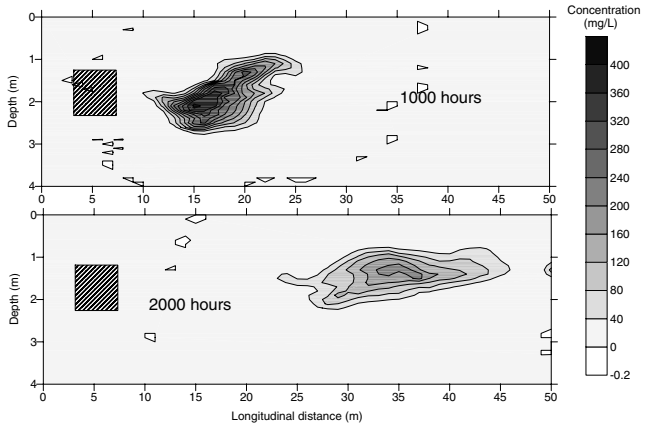

Fig. 3. Concentration contours in vertical cross section ($y = 9$ m), at $t = 0$, 1000 and 2000 h for a simulation of the Cape Cod tracer experiment. The Br^- tracer, at initial concentration 640 mg/l is transported in a heterogeneous velocity field from its initial position on the left side of the figure.

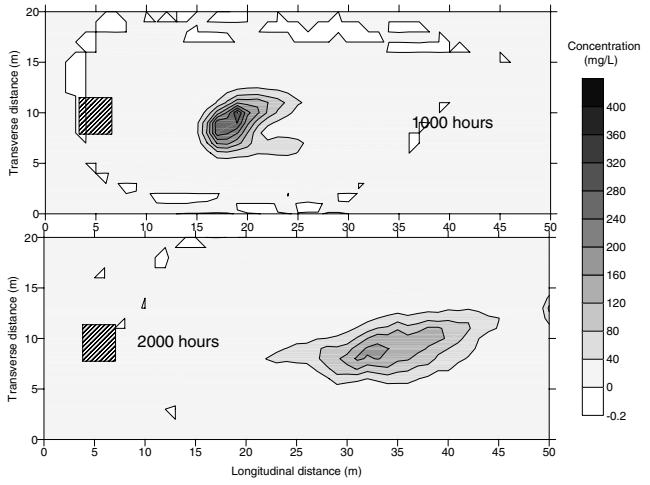

Fig. 4. Plan view of the Cape Cod tracer plume ($z = 1.6$ m) shown in Fig. 2.

m/day. This simulated velocity is lower than that obtained from field observations of the plume (0.424 m/day). The reason for this discrepancy is that the single realization of the random conductivity field employed had a geometric mean conductivity of 3.74 m/day instead of the field observed 3.96 m/day. If the code were used in a Monte Carlo simulation, then the mean simulated velocity should match that observed in the field.

Fig. 5 shows the time evolution of the second moments of the plume. The figure shows the moments calculated for both the coarse grid ($50 \times 20 \times 50$) and refined grid ($100 \times 40 \times 100$) using filled and hollow symbols, respectively. While there is only a small difference between the fine and coarse grid simulation in the longitudinal direction, there is a larger difference in the transverse direction, suggesting that further refinement would be required to obtain completely converged

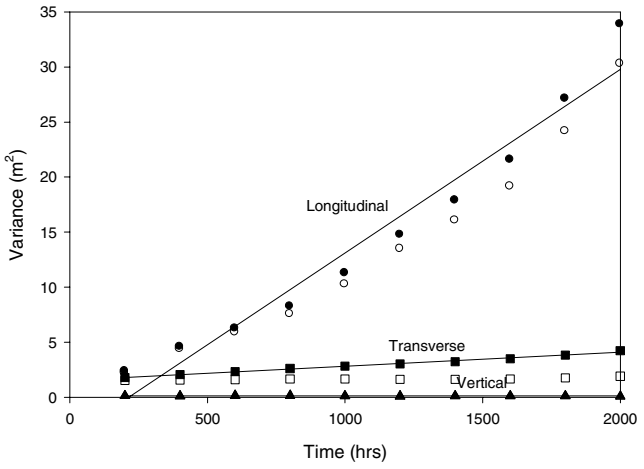

Fig. 5. Second moments of the modeled Cape Cod contaminant plume as a function of time. Filled symbols are for the $50 \times 20 \times 50$ grid and the hollow symbols are for the refined $100 \times 40 \times 100$ grid.

results in the transverse directions. As discussed by Garabedian [16], the calculated longitudinal dispersion increases with distance. This observation is consistent with stochastic theories. If the mean gradient of the variance curve is calculated, the simulated macrodispersivity can be calculated [16]. Table 3 gives the results for the coarse grid solution and shows a reasonable match between the field observed and simulated macrodispersivities. In the table, we provide computed dispersivities averaged over the entire simulation time as well as values based on late-time moments. These late-time values correspond to asymptotic dispersivities, which are directly comparable to the field estimates.

The zeroth moment of the plume is also calculated to confirm the mass balance accuracy of the code. In this case, the error in modeled contaminant mass remains less than 0.01% (0.0067% when 400,000 cells are used) for the duration of the simulation. The small mass balance errors are due to the use of numerical integration of the initial (C^0) concentration function.

The coarse grid simulation presented required 10 min to complete on PII 300 MHz computer. It is therefore feasible to do Monte Carlo simulation and computational experiments to illustrate stochastic groundwater

Table 3
Dispersivity coefficients calculated from the second moments of the simulated contaminant plume shown in Fig. 5 and as calculated by Garabedian [16] in his analysis of the Cape Cod field data

	Simulated (late time)	Field observation
Longitudinal dispersivity α_L (m)	0.586 (1.162)	0.96
Transverse dispersivity α_T (m)	0.045	0.018
Vertical dispersivity α_V (m)	≈ 0.0	0.015

The longitudinal dispersivity is also calculated at late time since it is increasing as a function of time in Fig. 5.

theories. The computational cost of these types of simulations have previously been prohibitive.

5. Conclusions

The ELLAM was applied for the first time to 3D problems in [6,24]. Here further details of the method of [6] are presented. The method has been shown to be a highly efficient and accurate solver for modeling contaminant concentration distributions. To illustrate this, the method was tested against analytical solutions and used for the computationally demanding problem of predicting contaminant transport in random velocity fields. In this case, the flow field was generated using random field material properties and a flow simulator similar to the popular USGS groundwater flow code MODFLOW. The Cape Cod simulation presented shows that the ELLAM can be employed to perform efficient simulations of stochastic groundwater problems.

To implement the ELLAM solver requires approximately 1700 lines of generously commented and spaced computer code. This code is considerably simpler, and easier to debug and maintain than previous ELLAM implementations by the current authors. For example, the 2D ELLAM code of Binning and Celia [5] required approximately 6000 lines of code. Inherently, the new code is very similar to widely used particle tracking and method of characteristics codes. We hope this advancement in the ELLAM procedure will lead to its wider adoption in practice.

In addition to the practical issues, the choice of form for the test function has been investigated with linear test functions being compared with the finite volume formulation [22] in particle tracking ELLAMs. The results suggest that when small numbers of integration points are employed, the linear test functions should be preferred as they are less sensitive to the oscillations found in the finite volume solution. The oscillations are caused by the jump discontinuities in the finite volume test function and the discrete sampling of the integration points. In contrast, the linear test functions are continuous and centrally weighted and so are less prone to such oscillations. The primary advantage of the finite volume formulation is that it strictly enforces local mass conservation while the linear test functions only achieve global mass conservation. Despite this advantage, the better behavior of the linear test functions suggests that this formulation has practical computational advantages. In addition to examining the choice of test function, the results presented have also shown that the accuracy of the ELLAM can be substantially improved using temporal lumping.

The ELLAM has been applied here and by Heberton and Russell [24,25] to 3D problems. With the recent resolution of the problem of handling sources and sinks [23], the ELLAM is now a mature method for the solution of the classical contaminant transport equation. For this problem, the method has been shown [39] to be competitive with other solution techniques. This suggests that the ELLAM may be successfully applied to other hyperbolic systems. However, the application of the ELLAM to nonlinear problems (e.g. shocks) and reactive systems remains an on-going challenge. There is much to be gained by moving beyond method-of-lines approaches that separate space and time approximations. The ELLAM unifies space–time approximations in a single theoretical framework, and provide efficient numerical solutions for practical problems.

Acknowledgements

The authors would like to thank the reviewers for their suggestions and comments.

References

[1] Aldama AA, Arroyo V. An Eulerian–Lagrangian localized adjoint method for the non-linear advection–diffusion–reaction equation. In: Burganos VN et al., editors. 12th International Confrence on Computational Methods in Water Resources. Crete Greece: Computational Mechanics Publications; 1998.

[2] Arbogast T, Wheeler MF. A characteristics-mixed finite element method for advection dominated transport problems. SIAM J Numer Anal 1995;32(2):404–25.

[3] Baptista AM. Solution of advection-dominated transport by Eulerian–Lagrangian methods using the backwards method of characteristics. PhD Thesis, MIT, Cambridge, MA, 1987.

[4] Binning P, Celia MA. Two-dimensional Eulerian–Lagrangian localized adjoint method for the solution of the contaminant transport equation in the saturated and unsaturated zones. In: Peters A, Wittum G, Herrling B, Meissner U, Brebbia CA, Gray WG, Pinder GF, editors. X International Conference on Computation Methods in Water Resources. Heidelberg, Germany: Kluwer Academic Publishers; 1994.

[5] Binning P, Celia MA. A finite volume Eulerian–Lagrangian localized adjoint method for solution of the contaminant transport equations in two-dimensional multiphase flow systems. Water Resour Res 1996;32(1):103–14.

[6] Binning P, Celia MA. A three-dimensional forward particle tracking Eulerian–Lagrangian localized adjoint method for solution of the contaminant transport equation. In: Bentley LR, Sykes JF, Brebbia CA, Gray WG, Pinder GF, editors. XIII International Conference on Computational Methods in Water Resources. Calgary: A.A. Balkema; 2000.

[7] Boris JP, Book DL. Flux corrected transport fluid. 1. SHASTA, a transport algorithm that really works. J Comput Phys 1973;11:38–69.

[8] Celia MA, Kindred JS, Herrera I. Contaminant transport and biodegradation: 1. A numerical model for reactive transport in porous media. Water Resour Res 1989;25:1148–411.

[9] Celia MA, Russell TF, Herrera I, Ewing RE. An Eulerian–Lagrangian localized adjoint method for the advection–diffusion equation. Adv Water Resour 1990;13(4):187–206.

[10] Celia MA, Zisman S. A Eulerian–Lagrangian localised adjoint method for reactive transport in groundwater. In: Gambolati VG,

Rinaldo A, Brebbia CA, Gray WG, Pinder GF, editors. Eighth International Conference on Computational Methods in Water Resources. Boston: Computational Mechanics Publications; 1990.
[11] Dahle HK, Ewing RE, Russell TF. Eulerian–Lagrangian localized adjoint methods for a nonlinear advection–diffusion equation. Comput Meth Appl Mech Eng 1995;122:223–50.
[12] Daus AD, Frind EO, Sudicky EA. Comparative error analysis in finite element formulations of the advection–dispersion equation. Adv Water Resour 1985;8(June):86–95.
[13] Douglas J, Pereira F, Yeh LM. A locally conservative Eulerian–Lagrangian numerical method and its application to nonlinear transport in porous media. Comput Geosci 2000;4(1):1–40.
[14] Douglas Jr. J, Russell TF. Numerical methods for convection-dominated diffusion problems based on combining the method of characteristics with finite elements or finite difference procedures. SIAM J Numer Anal 1982;19(5):871–85.
[15] Espedal MS, Ewing RE. Characteristic Petrov–Galerkin subdomain methods for two-phase immiscible flow. Comput Meth Appl Mech Eng 1987;64:113–35.
[16] Garabedian SP, LeBlanc DR, Gelhar LW, Celia MA. Large scale natural gradient tracer test in sand and gravel, Cape Cod, Massachusetts. 2. Analysis of spatial moments for a nonreactive tracer. Water Resour Res 1991;27(5):911–24.
[17] Goode DJ. Particle velocity interpolation in block-centred finite difference groundwater flow models. Water Resour Res 1990;26(5):925–40.
[18] Gray WG, Leijse A, Kolar RL, Blain CA. Mathematical tools for changing spatial scales in the analysis of physical systems. Boca Raton: CRC Press; 1993.
[19] Harbaugh AW, McDonald, MG. Users documentation for MODFLOW-96, an update to the US Geological Survey modular finite-difference groundwater flow model. US Geological Survey, 1996.
[20] Harten A. High resolution schemes for hyperbolic conservation laws. J Comput Phys 1983;49:357–93.
[21] Healy RW, Russell TF. A finite volume Eulerian–Lagrangian localized adjoint method for the solution of the advection–diffusion equation. Water Resour Res 1993;29(7):2399–413.
[22] Healy RW, Russell TF. Solution of the advection–dispersion equation in two dimensions by a finite-volume Eulerian–Lagrangian localized adjoint method. Adv Water Resour 1998;21(1):11–26.
[23] Healy RW, Russell TF. Treatment of internal sources in the finite-volume ELLAM. In: Bentley LR, Sykes JF, Brebbia CA, Gray WG, Pinder GF, editors. XIII International Conference on Computational Methods in Water Resources. Calgary: A.A. Balkema; 2000.
[24] Heberton CI, Russell TF, Konikow LF, Hornberger GZ. Three-dimensional finite volume ELLAM implementation. In: Bentley LR, Sykes JF, Brebbia CA, Gray WG, Pinder GF, editors. XIII International Conference on Computational Methods in Water Resources. Calgary: A.A. Balkema; 2000.
[25] Heberton CI, Russell TF, Konikow LF, Hornberger GZ. A three-dimensional finite-volume Eulerian–Lagrangian localized adjoint method (ELLAM) for solute-transport modelling. USGS Water Resources Investigations Report 00-4087, Reston, Virginia, 2000.
[26] Herrera I, Ewing RE, Celia MA, Russell TF. Eulerian–Lagrangian localized adjoint methods: the theoretical framework. Numer Meth Partial Diff Eqns 1993;9:431–57.
[27] Hess K, Wolf SH, Celia MA. Large-scale natural gradient tracer tests in sand and gravel, Cape Cod, Massachusetts 3. Hydraulic conductivity variability and calculated macrodispersivities. Water Resour Res 1992;28(8):2011–27.
[28] Hughes TJR, Brooks A. A theoretical framework for Petrov–Galerkin methods with discontinuous weighting functions: application to the streamline-upwinding procedure. In: Gallagher RH, editor. Finite elements in fluids. New York: Wiley; 1982. p. 47–65.
[29] Leblanc DR, Garabedian SP, Hess KM, Gelhar LW, Quadri RD, Stollenwerk KG, Wood WW. Large scale natural gradient tracer test in sand and gravel, Cape Cod, Massachusetts 1. Experimental design and observed tracer movement. Water Resour Res 1991;27(5):895–910.
[30] Leije FJ, Skaggs TH, Genuchten MTV. Analytical solutions for solute transport in three-dimensional semi-infinite porous media. Water Resour Res 1991;27(10):2719–33.
[31] Morton KW, Priestley AW, Suli E. Stability of the Lagrangian–Galerkin method with non-exact integration. RAIRO Model Math Anal Numer 1988;22(123).
[32] Ogata A, Banks RB. A solution of the differential equation of longitudinal dispersion in porous media. USGS Geological Survey Professional Papers 411-A, 1961.
[33] Pironneau O. On the transport–diffusion algorithm and its application to the Navier–Stokes equations. Numer Math 1982;38:309–32.
[34] Russell TF, Trujillo RV. Eulerian–Lagrangian localized adjoint methods with variable coefficients in multiple dimensions. In: Gambolati G, Rinalto A, Brebbia CA, Gray WG, Pinder GF, editors. VIII International Conference on Computer Methods in Water Resources. Italy: Venice; 1990.
[35] Tompson AFB, Ababou R, Gelhar LW. Implementation of the three-dimensional turning bands random field generator. Water Resour Res 1989;25(10):2227–43.
[36] Varoglu E, Finn WDL. Finite elements incorporating characteristics for one-dimensional diffusion–convection equation. J Comput Phys 1980;34:371–89.
[37] Wang H, Dahle HK, Ewing RE, Espedal MS, Sharpley RC, Man S. An ELLAM scheme for advection–diffusion equations in two-dimensions. SIAM J Sci Comput 1999;20:2160–94.
[38] Wang H, Ewing RE, Celia MA. Eulerian–Lagrangian localized adjoint method for reactive transport with biodegradation. Numer Meth PDEs 1995;11:229.
[39] Wang H, Ewing RE, Qin G, Lyons SL, Al-Lawatia M, Man S. A family of Eulerian–Lagrangian localized adjoint methods for multi-dimensional advection–reaction equations. J Comput Phys 1999;152:120–63.
[40] Wang H, Liang D, Ewing RE, Lyons SL, Qin G. An accurate simulator of compressible flow in porous media with wells. In: Bentley LR, Sykes JF, Brebbia CA, Gray WG, Pinder GF, editors. XIII International Conference on Computational Methods in Water Resources. Calgary: A.A. Balkema; 2000.
[41] Wood WW, Kraemer Jr. TF. PPH intergranular diffusion: an important mechanism influencing solute transport in clastic aquifers. Science 1990;247(4950):1569–72.
[42] Zhang H, Schwartz FW, Wood WW, Garabedian SP, LeBlanc DR. Simulation of variable density flow and transport of reactive and non-reactive solutes during a tracer test at Cape Cod, Massachusetts. Water Resour Res 1998;34(1):67–82.